Low Temperature Physics/Fizika Nizkikh Temperatur, 2014, v. 40, No. 4, pp. 426–438

Probing the Fermi surface by positron annihilation and Compton scattering

S.B. Dugdale

H.H. Wills Physics Laboratory, University of Bristol, Tyndall Avenue, Bristol BS8 1TL, United Kingdom
E-mail: S.B.Dugdale@bristol.ac.uk

Received December 2, 2013

Positron annihilation and Compton scattering are important probes of the Fermi surface. Relying on conservation of energy and momentum, being bulk sensitive and not limited by short electronic mean-free-paths, they can provide unique information in circumstances when other methods fail. Using a variety of examples, their contribution to knowledge about the electronic structure of a wide range of materials is demonstrated.

PACS: **71.18.+y** Fermi surface: calculations and measurements; effective mass, *g*-factor;
78.70.Bj Positron annihilation;
78.70.–g Interactions of particles and radiation with matter.

Keywords: Compton scattering, electronic structure, positron annihilation.

1. Introduction

Positron annihilation and Compton scattering are two closely related experimental techniques which can be used to investigate the Fermi surface topologies of materials. Relying only on the conservation of energy and momentum, these methods are not restricted by short electronic mean-free-paths and probe the bulk (as opposed to the surface) which means that they can provide vital information about the electronic structure of materials in which quantum oscillatory (for example, via the de Haas-van Alphen (dHvA) effect) measurements or angle-resolved photoemission spectroscopy (ARPES) experiments have had limited (or even no) success. The precision with which the Fermi surface can be determined using either positron annihilation or Compton scattering is, however, significantly lower than that afforded by either an angle-resolved photoemission experiment or the measurement of quantum oscillations, and doesn't provide any further complementary information (for example, concerning quasiparticle masses, or the band structure dispersion) which is available by these methods. Nevertheless, in circumstances where these other methods are precluded (for example, in substitutionally disordered alloys, high temperature phases or materials which do not easily cleave or in which the surface is not representative of the bulk) then positron annihilation and Compton scattering provide an important viable alternative.

Rather than being an exhaustive review of the field, this paper aims to showcase the positron and Compton techniques with an emphasis on what complementary information they can bring to the field of Fermi surface measurements across a diverse range of materials.

2. Electron momentum densities and the measurement of the Fermi surface

The electron momentum distribution (EMD), $\rho(\mathbf{p})$, can be expressed as

$$\rho(\mathbf{p}) = \sum_{\text{occ.}\mathbf{k},j} |\int d\mathbf{r}\psi_{\mathbf{k},j}(\mathbf{r})\exp(-i\mathbf{p}.\mathbf{r})|^2 =$$
$$= \sum_{\text{occ.}\mathbf{k},j,\mathbf{G}} |B_j(\mathbf{k}+\mathbf{G})|^2\ \delta(\mathbf{p}-\mathbf{k}-\mathbf{G}),$$

where $\psi_{k,j}(\mathbf{r})$ is the wave function of an electron in band j, and $B_j(\mathbf{k}+\mathbf{G})$ are the Fourier coefficients of the electron wavefunction, and the δ function expresses the conservation of crystal momentum.

This EMD is a single-centre distribution in **p**-space which just has the point symmetry of the crystal. It can, however, be transformed into a distribution which has the translational invariance of the underlying reciprocal lattice using the so-called Lock–Crisp–West (LCW) theorem [1] which prescribes a further sum over reciprocal lattice vectors :

$$\sum_{\mathbf{G}'}\rho(\mathbf{p}+\mathbf{G}') = \sum_{\mathbf{G}'}\sum_{\text{occ.}\mathbf{k},\mathbf{G},j} |B_j(\mathbf{k}+\mathbf{G})|^2\ \delta(\mathbf{p}-\mathbf{k}-\mathbf{G}+\mathbf{G}').$$

There is now a double summation over reciprocal lattice vectors which allows us to regroup the various terms which involve the same vector $\mathbf{G}'' = \mathbf{G} - \mathbf{G}'$. The δ-function, which originally redistributed the information in the first Brillouin zone out into higher zones, now has the effect of producing the same distribution about each reciprocal lattice point, i.e.

$$\sum_{\mathbf{G}'} \rho(\mathbf{p}+\mathbf{G}') = \sum_{\mathbf{G}''} \sum_{\text{occ.}\mathbf{k},\mathbf{G},j} |B_j(\mathbf{k}+\mathbf{G})|^2 \, \delta(\mathbf{p}-\mathbf{k}-\mathbf{G}'').$$

Since the the electron wavefunctions are normalized,

$$\sum_{\mathbf{G}} |B_j(\mathbf{k}+\mathbf{G})|^2 = 1,$$

and therefore in the first Brillouin zone we can write

$$\rho(\mathbf{k}) = \sum_j n^j(\mathbf{k}).$$

The shape of the Fermi surface can straightforwardly be inferred from the changes in the occupation function, $n^j(\mathbf{k})$ across the Brillouin zone.

3. Two-photon momentum densities and the measurement of the Fermi surface

The two-photon momentum density (TPMD), $\rho^{2\gamma}(\mathbf{p})$, sometimes referred to as the electron–positron momentum density, can be expressed as

$$\rho^{2\gamma}(\mathbf{p}) = \sum_{\text{occ.}\mathbf{k},j} \left| \int d\mathbf{r} \sqrt{\gamma(\mathbf{r})} \psi_{\mathbf{k},j}(\mathbf{r}) \psi_+(\mathbf{r}) \exp(-i\mathbf{p}.\mathbf{r}) \right|^2,$$

where $\psi_{k,j}(\mathbf{r})$ and $\psi_+(\mathbf{r})$ are the electron and positron wave functions, respectively, $\mathbf{G}$ is a reciprocal lattice vector, and $\gamma(\mathbf{r})$ is the so-called enhancement factor which takes account of electron–positron correlations (and would be unity in the independent particle model (IPM)) [2]. The problem of dealing with enhancement is an important one (and one which is still the subject of current studies [3,4]), but a proper treatment is beyond the scope of this review and discussions can be found elsewhere [2,5,6].

The application of the LCW theorem becomes

$$\sum_{\mathbf{G}'} \rho^{2\gamma}(\mathbf{p}+\mathbf{G}') = \sum_{\mathbf{G}''} \sum_{\text{occ.}\mathbf{k},\mathbf{G},j} |C_j(\mathbf{k}+\mathbf{G})|^2 \, \delta(\mathbf{p}-\mathbf{k}-\mathbf{G}''),$$

where the $C_j(\mathbf{k}+\mathbf{G})$ are the Fourier coefficients of the electron–positron wave function product. Writing $\chi^j(\mathbf{k}) = |C_j(\mathbf{k}+\mathbf{G})|^2$, within the first Brillouin zone,

$$\rho^{2\gamma}(\mathbf{k}) = \sum_j n^j(\mathbf{k}) \chi^j(\mathbf{k}).$$

Therefore, in the case of positron with a $\mathbf{k}$-dependent wavefunction, the electron occupancy is smoothly modulated by the $\chi^j(\mathbf{k})$ function. Since these smoothly varying modulations are quite different from the relatively large and sudden changes in occupancy when a band crosses the Fermi energy, the effect of the positron wavefunction is to slightly impede, but not prevent the measurement of Fermi surfaces.

4. Positron annihilation and Compton scattering

As we have seen from the previous section, both the electron and the two-photon momentum densities contain information about the Fermi surface. The three-dimensional densities are not themselves measured directly. Experimentally, the EMD is accessed via 1D projections known as Compton profiles ($J(p_z)$):

$$J(p_z) = \iint dp_x dp_y \rho(\mathbf{p}) \, .$$

Compton profiles are obtained from the energy distribution of inelastically scattered photons (typically x-rays from a synchrotron source). A variety of designs for high-resolution spectrometers have existed, but a description of a typical spectrometer, located at the SPring-8 synchrotron can be found in Refs. 7, 8.

In a Two Dimensional Angular Correlation of positron Annihilation Radiation (2D-ACAR) experiment, the angular distribution of γ-photons emanating from the electron–positron annihilation in the sample being studied is measured. The deviation from anti-collinearity of the two photons is measured by a pair of position-sensitive detectors which are located either side of the sample chamber, and this deviation is proportional to the momentum components of the annihilated electron–positron pair in the plane perpendicular to the spectrometer (detector–sample–detector) axis. The third momentum component would be expressed as a Doppler shift in the energy of the photons, but this is not usually measured. Therefore, the measured distribution, $N(p_x, p_y)$, is an integration of the TPMD over this component.

$$N(p_x, p_y) = \int dp_z \rho^{2\gamma}(\mathbf{p}) \, .$$

Different technologies have been used for the position sensitive detectors and descriptions of the detection systems in spectrometers currently in use (including the latest developments) can be found in Refs. 9–11.

5. Three dimensional reconstruction

Although a positron measurement yields a 2D projection (integration over one momentum component) of the underlying momentum density, and a Compton profile represents a 1D projection (integration over two momentum components), it is possible to use tomographic methods to reconstruct the full three dimensional density. In this context, the work of Kontrym–Sznajd deserves special mention. Building on the work of Cormack [12,13], Kontrym–Sznajd championed the so-called modified Cormack method of reconstruction [14], which has facilitated high-fidelity reconstructions of the Fermi surfaces of a variety of materials.

Measurement of sufficiently different 2D-ACAR projections or Compton profiles has to be balanced against the real time available to collect the data. The compromise is usually to settle, in the case of a positron experiment, for typically ~ 5 projections measured down different crystallographic directions. While there is much to be gained from measuring some special directions [15], in practice a mixture of high-symmetry and some lower symmetry directions are often measured. In this section some examples of three-dimensional reconstructions are presented, with the particular materials chosen to illustrate the quality of information which can be extracted.

5.1. Helical ordering in the rare-earths

The role of the so-called "webbing" Fermi surface [16] in driving the magnetic order in the heavy rare earths is, today, well established [17]. Positron annihilation was used right from the beginning of such investigations, with early calculations by Loucks including a calculation of the positron wavefunction [18]. In a series of positron annihilation experiments on Y and its alloys with Gd [19–21], Dugdale *et al.* were able to experimentally establish the existence of this webbing, show that the size of the vector which spanned the webbing could be linked with the magnetic ordering vectors when small amounts of rare earth were alloyed into Y [22], and monitor its evolution under doping.

In Fig. 1 this evolution is shown for pure Y and two different Gd–Y alloys. The webbing can be identified as the flat sections perpendicular to the c^* axis. Subsequent Compton scattering experiments by Kontrym–Sznajd *et al.* in Y [23] were in agreement with the earlier positron results.

5.2. $ZrZn_2$

At the time, the observation of superconductivity in $ZrZn_2$ [24,25] caused great excitement, following so soon after the discovery of triplet superconductivity in UGe_2 [26]. The shape of the Fermi surface was the focus of much attention [27,28], and measurements of de Haas–van Alphen oscillations in the ferromagnetic phase [29] and the paramagnetic Fermi surface by positron annihilation [24] revealed four separate sheets of Fermi surface (see Fig. 2) which were in excellent agreement with the predictions of band structure calculations. Although it was later found to be due to the spark erosion which led to superconductivity in a Zn-depleted surface layer [30], the paper of Major *et al.* [24] is an excellent example of the high quality information which can be extracted.

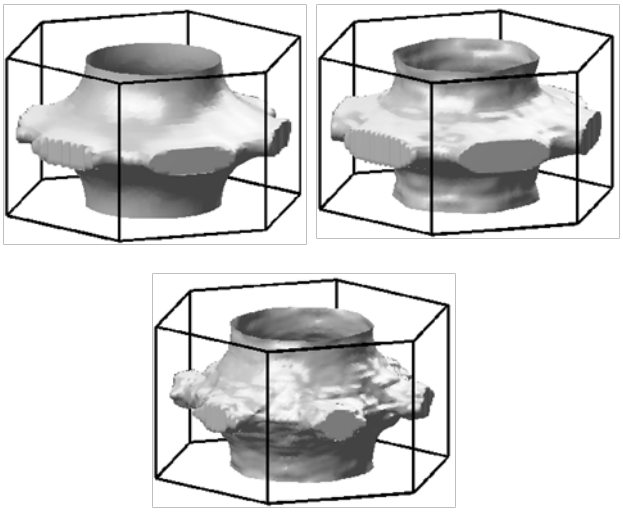

Fig. 1. Positron annihilation measurements of the FS topologies in pure Y (top left), $Gd_{0.62}Y_{0.38}$ (top right) and $Gd_{0.70}Y_{0.30}$ (bottom).

5.3. Compositional short-range order in $Cu_{1-x}Pd_x$ *alloys*

Diffuse scattering in x-ray and electron diffraction patterns measured in substitutionally disordered Cu–Pd alloys [31,32] has its origins in the nesting of the Fermi surface. Inspired by the calculations of Gyorffy and Stocks [33] which made a direct connection between the size and shape of the Fermi surface and the positions of the diffuse spots, Wilkinson *et al.* made a series of positron annihilation measurements in order to reconstruct the Fermi surface and investigate its nesting propensities [34].

The experimentally measured Fermi surface of $Cu_{0.6}Pd_{0.4}$ is shown in Fig. 3, and in Fig. 4 some slices through the measured Fermi surfaces are shown for the two different alloy concentrations, together with the theoretical predictions. It should be noticed how the Fermi surface of $Cu_{0.6}Pd_{0.4}$ has larger flat areas than $Cu_{0.72}Pd_{0.28}$, which make it better nested.

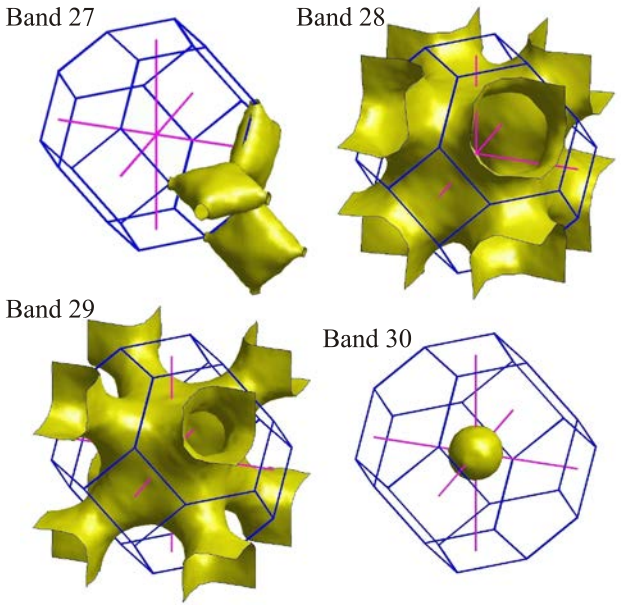

Fig. 2. (Color online) Positron annihilation measurements of the Fermi surface topology of paramagnetic $ZrZn_2$. The band numbering refers to the original paper [24] and note that all four sheets are clearly revealed.

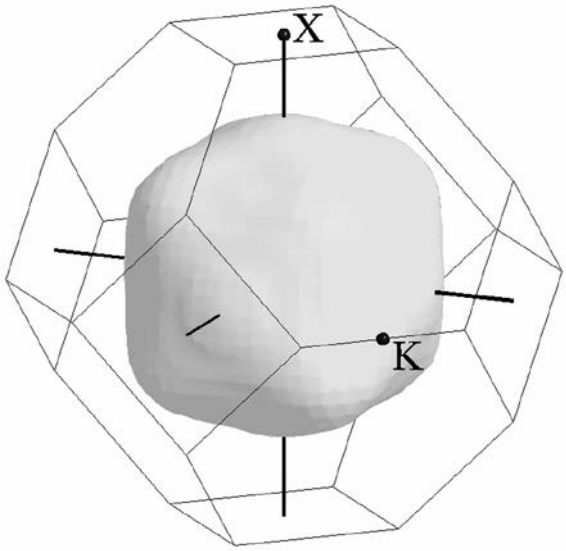

Fig. 3. The Fermi surface of $Cu_{0.6}Pd_{0.4}$, reconstructed from 2D-ACAR projections.

That the Fermi surface of $Cu_{0.6}Pd_{0.4}$ is much more nested than $Cu_{0.72}Pd_{0.28}$ explains not only the location of the diffuse scattering peaks [32] but also their relative intensity. Interestingly, the calculations which are performed within the mean-field coherent potential approximation [35], while not able to perfectly predict the real Fermi surfaces (for example, in the calculations they predict that the necks, familiar from the pure Cu Fermi surface, along the ⟨111⟩ directions are still present), are able to accurately predict both qualitatively and quantitatively the trends under doping. A similar conclusion was reached on the basis of a reconstruction from 28 directional Compton profiles in a $Cu_{0.75}Pd_{0.25}$ measured by Matsumoto *et al.* [36].

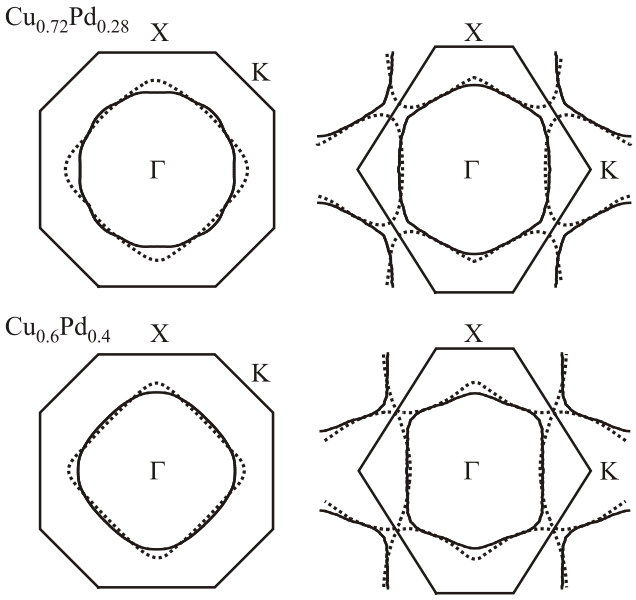

Fig. 4. (100) (left hand side) and (110) (right hand side) planes through the Fermi surface of $Cu_{0.72}Pd_{0.28}$ (top) and $Cu_{0.6}Pd_{0.4}$ (bottom). The solid lines represent the experimental data and the dashed lines the KKR–CPA calculation; the boundary and selected symmetry points of the first BZ are also shown.

6. Charge and spin-density waves

Charge- and spin-density wave systems have proven a fertile ground for positron annihilation experiments. In the presence of a density wave modulation, there will be an additional smearing (proportional to the size of the energy gap) in the momentum density discontinuity at the wavevector centred on the energy gap induced by the new periodic modulation [37]. This contribution, however, is of the order of, or even much smaller than, the smearing due to the instrumental resolution. The consequence, therefore, is that one is able to "see" the ungapped Fermi surface and thus investigate the role of the Fermi surface in the formation of that density wave.

6.1. Charge density waves in the tri-tellurides

It is almost half a century since Peierls pointed out that a one-dimensional metal coupled to its lattice was unstable [38]. The pioneering work of Wilson *et al.* in studying the connection between Fermi surface nesting and CDW formation in layered structures (e.g., [39]) was instrumental in laying the foundations for investigations of ever more electronically complex materials (such as $Lu_5Ir_4Si_{10}$ [40] or $RNiC_2$ [41]). More recently, Johannes and Mazin have carefully studied the connection between Fermi surface nesting and CDW formation in real materials, and emphasised that Fermi surface nesting is unlikely to be solely responsible in most cases [42]. Moreover, they emphasised the importance of verifying that peaks in the imaginary part of the generalized susceptibility carry through into the real part at the correct wavevector if the Fermi surface is to be held accountable. The work of Laverock *et al.* in 2H-$TaSe_2$ which combined ARPES with a tight-binding band structure fitted to the data, has shown just how subtle (and unconventional) the role of the Fermi surface can be [43].

The rare-earth tritellurides (RTe_3) have, over the past decade, become an important prototype system for the study of charge-density waves (CDWs), and are an excellent example of a material where important information can be obtained from positron annihilation. With the compounds stable for rare earths from La to Tm, they represent a model system for studying the interactions between the electrons and the lattice, for example by using chemical pressure [44]. Moreover, angle-resolved photoemission is unable to see the parts of the Fermi surface gapped by the CDW [45,46]. In Fig. 5, the calculated Fermi surface of $LuTe_3$ is shown, along with a nesting vector which matches the experimentally observed incommensurate order [47]. Note that Lu was chosen to avoid problems describing the f states within the LDA, and this non-f-electron re-

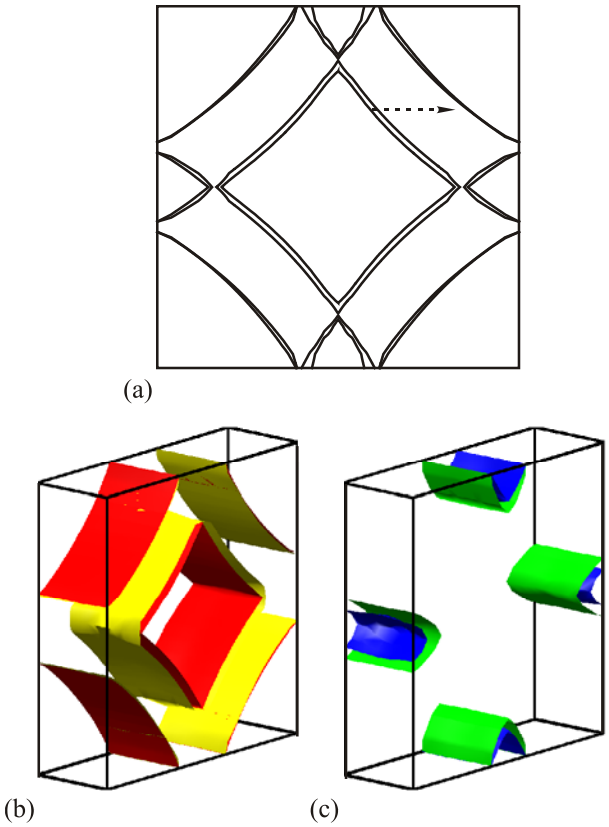

Fig. 5. (Color online) Fermi surface of $LuTe_3$ calculated (a) on a (010) plane through Γ with an arrow marking $2/7c^*$. The outer FS sheets (b). The inner FS sheets (c).

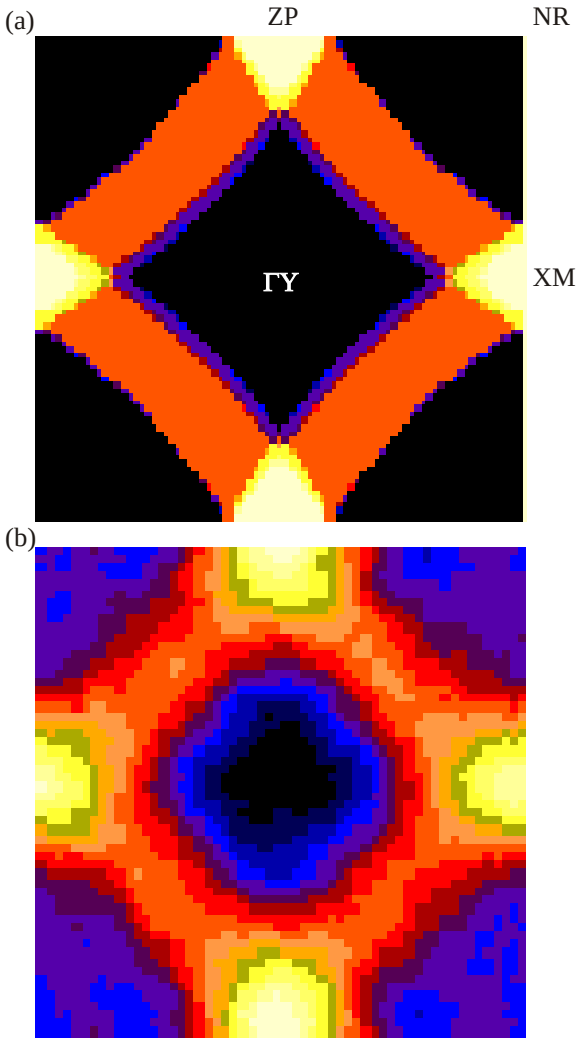

Fig. 6. (Color online) Occupancy within the Brillouin zone obtained (a) from the $LuTe_3$ calculation, and (b) from the positron experiment on $TbTe_3$. White represents high occupancy and black represents low occupancy.

ference should provide an accurate description given that the electrons in the partly filled f band are, in fact, rather localized and below the Fermi energy.

In Fig. 6, the positron annihilation measurement of the (b^*-axis) Fermi surface of $TbTe_3$ is shown, together with the occupancy from the $LuTe_3$ calculation [48]. Given the strong two-dimensionality of the electronic structure, the projected nature of the positron experiment is not a serious drawback. The nesting vector extraced from the positron experiment was found to be $(0.28 \pm 0.02, 0, 0)(2\pi/a)$, in excellent agreement with the modulations inferred from electron diffraction [47].

6.2. The spin-density wave of Cr

Cr exhibits a famous phase transition at 311.5 K from a paramagnetic (PM) to an antiferromagnetic (AFM) phase, in which the ordering of the magnetic moments is slightly incommensurate with the underlying lattice [49]. This was explained originally with the Overhauser mechanism [50,51] by the nesting of Lomer's calculated paramagnetic Fermi surface [52]. Specifically, the shapes and sizes of the electron and hole octahedra, centered at the Γ and H points of the Brillouin zone are almost identical, leading to an almost perfect nesting.

The earliest momentum density experiments on Cr were 1D-ACAR [53] measurements which were difficult to interpret directly in terms of the Fermi surface topology due to the doubly integrated nature of the measurement. Moreover, they reported no difference in the spectra measured in the PM and AFM phases. Given the high transition temperature, the paramagnetic phase is out of the reach of quantum oscillatory experiments. The first positron annihilation experiment to show a difference between data measured in the PM and AFM phases was that of Singh, Manuel, and Walker [54].

The first three-dimensional reconstruction of the momentum density and Fermi surface in Cr was by Kubota *et al.* [55], followed a few years later by Fretwell *et al.* who emphasized the advantages for deconvoluting the measured spectra prior to reconstruction [56,57]. One of the particularly perplexing issues was that the comparison of the experimental Cr spectra with theory, for both the

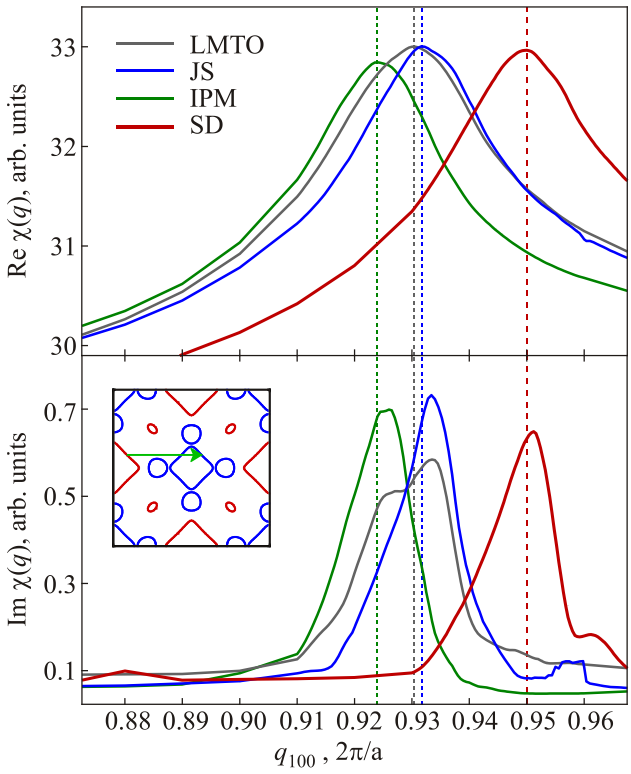

Fig. 7. (Color online) The real (top) and imaginary (bottom) parts of the static susceptibility, $\chi^0(q)$, of paramagnetic Cr, calculated for the raw band LMTO calculations as well as the results of the rigid-band fit to the data with the independent particle model (IPM), Jarlborg–Singh (JS, [2]) and state-dependent (SD, [4]) models of enhancement. The dashed vertical line represents the peak in the real part of the susceptibility. The inset shows a slice of the FS through the (001) plane, with the arrow depicting the nesting that gives rise to the peak in Im $\chi^0(q)$ between the hole (outer) and electron (inner) FS sheets.

positron annihilation measurements [58] and later Compton scattering [59,60], was always substantially less favorable than the comparison between measurement and theory in Sec. 5. Positron measurements in Mo, which being isoelectronic to Cr was thought to possess a very similar Fermi surface, conversely agreed very well with theoretical predictions [58]. The eventual explanation for this came much more recently, when Laverock *et al*. showed that the discrepancy came from a combination of inadequacies in the description of the electron–positron interaction (the so-called enhancement) and a real difference in the band structure [4]. Laverock *et al.* were also able to show (Fig. 7) that a band structure tuned to the experimental data was able to predict a peak in the generalized susceptibility at a wavevector which matched the small incommensurability of the spin-density wave in Cr, highlighting both the role of the Fermi surface and the power of the positron technique in being able to deliver such precise information [4].

The power of the technique for revealing evolutionary trends in the topology of the Fermi surface under different dopings in substitutionally disordered alloys was demonstrated in the work of Hughes *et al.* [61]. The primary objective of that work was to identify which particular part of the Fermi surface was responsible for mediating (via an RKKY-type interaction) the oscillatory exchange coupling in the non-magnetic spacer layers in magnetic multilayers [62,63]. These spacer layers included Cr and its alloys with V and, on the basis of an extensive measurement programme, it was possible to reveal that the N-hole Fermi surface pockets evolved with doping in a manner consistent with the observed oscillation periods.

7. Heavy fermions

The question of the degree of f-electron localization in rare-earth compounds is intimately connected with the strength of electron–electron correlations. From the perspective of density-functional theory, and in particular the commonly used local density approximation (LDA) to the exchange-correlation functional, accurate descriptions of the electronic structure of f electron systems pose a challenge. One of the important questions in heavy fermion physics is whether the f electrons become itinerant and contribute to the Fermi surface below some temperature characteristic of the heavy fermion state, known as the coherence temperature. With its ability to probe as a function of temperature, and its insensitivity to the quasiparticle mass (in contrast to quantum oscillations, where heavy orbits are more difficult to see, needing high magnetic fields), positron annihilation has been able to shed some light on this problem.

7.1. $CeIn_3$

The value of the positron annihilation technique in heavy fermion physics is typified by the comprehensive study of the three-dimensional antiferromagnetic superconductor $CeIn_3$ in its paramagnetic phase by Biasini *et al.* [64]. Five separate spectra were collected with integration directions between the [100] and [110] crystallographic directions, and these were then used to tomographically reconstruct the three dimensional momentum density, and LCW-folded occupancies within the first Brillouin zone. The theoretical model in which the f electrons were treated as localized core states produced a Fermi surface which was unambiguously more consistent with the positron experiment. When their 3D data were LCW-folded according the AF until cell (to simulate what might be observed in the AF phase), a Fermi surface emerges which is consistent with dHvA measurements [65] in the antiferromagnetic phase, leading Biasini *et al.* to conclude that the f electrons remain localized. This conclusion has, however, been challenged by recent (dynamical mean field theory, DMFT) calculations [66].

7.2. $CeRu_2Si_2$ and $LaRu_2Si_2$

Comparisons between Ce-containing heavy fermions and their non-f La counterparts can be very useful in isolating the behavior of the f electrons. $CeRu_2Si_2$ is often considered to be the archetypal heavy fermion system [67], and Monge *et al.* [68] performed positron annihilation experiments in both that compound and $LaRu_2Si_2$. De Haas–van Alphen experiments in $CeRu_2Si_2$ [69] at temperatures well below the Kondo temperature ($T_K \sim 20$ K) seemed to indicate that the f electrons were itinerant. As in $CeIn_3$, five projections were measured at a temperature of 60 K (above T_K) with integration directions between the [100] and [110] crystallographic directions prior to tomographic reconstruction of the 3D momentum densities and then Fermi surfaces in both compounds. By comparing their data for the Ce compound with LDA calculations in which the f electrons were either localized or itinerant, and with $LaRu_2Si_2$, they were able to determine that the localized description was appropriate. This careful comparison further showed that a rigid upward shift of the Fermi energy by 11mRy (~ 0.15 eV) was necessary to bring the theoretical calculation for $LaRu_2Si_2$ into agreement with experiment. This kind of shift (albeit for individual bands, rather than a global shift) was found to be necessary recently in Fermi surface measurements in the Fe-pnictide superconductors on the basis of quantum oscillations [70] and Compton scattering [71], and has also been found to be necessary to accurately reproduce Fermi surfaces in other materials [72,73]. As Monge *et al.* pointed out, however, if such shifts are necessary even without the complexities introduced by f electrons, it does call into question the assertion, based on such LDA calculations and dHvA data [69,74], that the f electrons are itinerant in the heavy fermion state.

7.3. $CeCu_2Si_2$

In contrast to the localized f-electron picture in $CeRu_2Si_2$, the positron annihilation experiments of Vasumathi *et al.* which probed the Fermi surface of $CeCu_2Si_2$ indicated that f-electrons are itinerant, but to a lesser extent than predicted by LDA calculations [75]. By shifting the f bands relative to the Fermi energy they found a better agreement between calculation and experiment, and the effect of the band shift was to decrease the f-electron population.

8. Confined positrons in precipitates

It is possible to take full advantage of the positron's preference for a particular annihilation environment (its so-called affinity, defined as the difference between the internal electron and positron chemical potentials [76]) to create a powerful probe in which the positrons behave like "magic bullets". Simply put, in some heterostructure made from different components, the positron affinity will indicate the preference for the positron for one component over another. Thus, if the positron affinity is greater for a precipitate rather than the host matrix, then the positron will show a preference for annihilation within the precipitate. This has been referred to as an affinity-induced quantum-dot-like state [77]. Early positron experiments showed that positrons could indeed be confined within nano-, and even subnano-sized particles of Cu embedded within a dilute Fe–Cu alloy, and that these ultrafine particles had the momentum distribution very similar to bulk Cu [78]. Subsequent 2D-ACAR experiments on Cu nanocrystals embedded in Fe, prepared by the thermal aging of a single crystal of a Fe–1.0 wt.% Cu alloy, were able to reveal the Fermi surface of bcc Cu with necks reaching out to the {110} Brillouin zone boundaries [84]. Inspired by the classical Hume–Rothery rules which come from the interaction of the Fermi surface with the Brillouin zone boundary, Nagai *et al.*'s essential idea was that a given precipitate will adopt whatever lattice structure avoids it having to occupy the electronic states which are in the higher energy band, which means that a stable precipitate in a given matrix structure will adopt its chemical composition to give an optimized electron per atom ratio. The formation of Fermi surface necks will, quite generally, cause a reduction in the total electronic energy due to the interaction of the electronic states with the zone boundary (the so-called "band-gap" effect). Nagai *et al.* went on to outline a general approach for predicting the chemical composition of solute nanoclusters which are coherent to a matrix with nearly free electrons (such as Al, for example) [79]. Using Ag-rich and Zn nanoclusters within an Al matrix as examples, and with *ab initio* calculations of the anisotropies of the momentum distributions of possible chemical compositions with different structures (e.g., fcc Zn, $L1_2$ Al_3Ag, $L1_0$ AlAg, $L1_2$ $AlAg_3$) they were able to show that examining the experimental data for the presence of Fermi surface necks was the key to identifying the chemical composition. Toyama *et al.* were able to use the additional smearing of the Fermi surface due to finite-size effects to estimate the size of embedded nano-precipitates [80].

Owing to their technological use in aerospace applications, Al alloys have a special importance. Alloying with small amounts of Li (in the range of 5–25%) results in a stronger, lighter alloy with the formation of metastable δ' precipitates. These precipitates are in fact highly ordered $L1_2$ Al_3Li which is coherent with the parent fcc Al matrix with only a small lattice mismatch [81,82]. Using the positron's affinity for the precipitates, the Fermi surface of Al_3Li was determined using positron annihilation on an Al–9 at.% Li sample by Laverock *et al.* [83]. Four different crystallographic projections were measured (see Fig. 8) and, informed by *ab initio* calculations Laverock *et al.* were able to determine that all positrons were trapped within and annihilated from the Al_3Li δ' precipitates. The data pre-

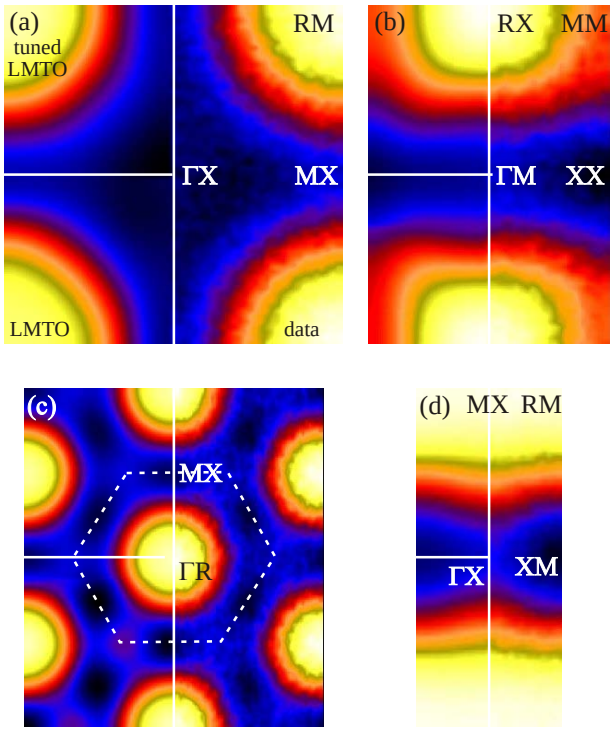

Fig. 8. (Color online) Positron annihilation data in the first BZ for Al–9 at.% Li, shown in the right panel of each figure, projected along the [100] (a), the [110] (b), the [111] (c) and the [210] (d) crystallographic directions. The high-symmetry points in projection have been labelled for each direction, and the projected BZ is marked in (c). In the bottom left panel, the independent particle model electron-positron momentum density from the LMTO calculation is shown, and the tuned calculation (see [4,83]) is presented in the top left panel. All theoretical distributions have been convoluted with the experimental resolution function.

sented in Fig. 8, where comparison is made with theoretical calculations made within the independent particle model, and within the empirical state-dependent enhancement approach developed by Laverock *et al.* [4], are compatible with the Fermi surface predicted by the band structure of Guo *et al.* [84].

9. Shape memory alloys

The shape memory phenomenon is associated with a martensitic transformation, a diffusionless solid–solid phase transition which itself is often associated with a soft phonon mode. When the martensitic transformation occurs as a function of temperature, pre-martensitic phenomena (for example an incomplete softening of a phonon mode) are sometimes observed at substantially higher temperatures, and there is considerable evidence that Fermi surface nesting is responsible. Moreover, these premartensitic phenomena are considered to be precursors of the soon-to-be incipient martensitic transition.

Although substitutional disorder makes the observation of quantum oscillations very difficult (or even impossible), de Haas–van Alphen measurements have been able to make important contributions in the ordered AuZn [85,86]. However, many of the alloys are substitionally disordered, or experiments are excluded because the relevant phase occurs at high temperature. Furthermore, positron annihilation experiments are made more difficult, but not excluded (see the Ni_2MnGa results below) by single crystals which seem to be more prone to higher vacancy concentrations (which trap the positrons and suppress the signal).

9.1. $Ni_{1-x}Al_x$

Kohn anomalies [87] driven by nestable regions on the Fermi surface impacting on the electronic screening (and hence on the electron–phonon coupling) were initially suggested as the origin of the premartensitic phenomena (such as premartensitic phonon softening [88]) by Zhao and Harmon [89]. Given the disordered nature of the alloys, the degree to which the Fermi surface remains a well-defined, sharp entity is an important consideration. KKR–CPA calculations [90] indicate, however, that the nested part in $Ni_{1-x}Al_x$, identified by Zhao and Harmon, remains rela-

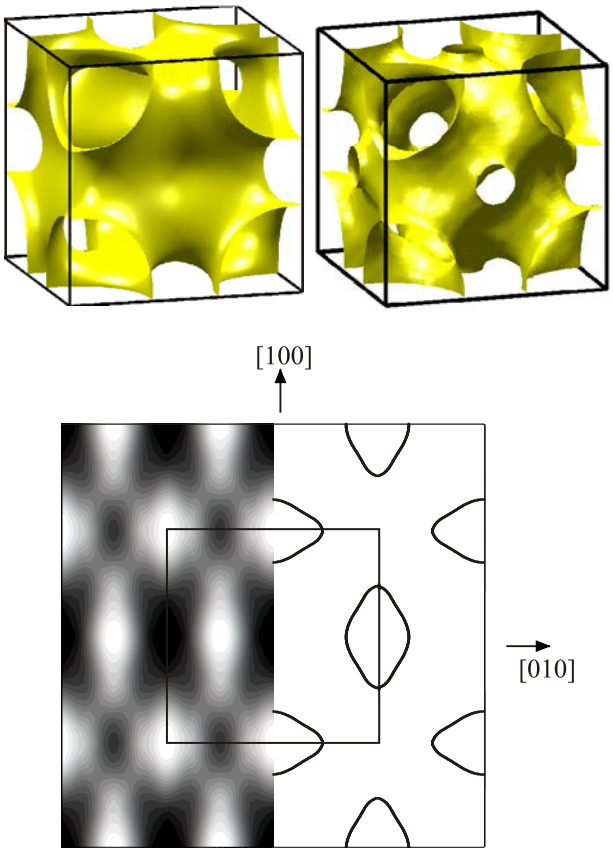

Fig. 9. (Color online) $Ni_{0.62}Al_{0.38}$. Fermi surface predicted by KKR–CPA calculations (top left) and that reconstructed from a Compton scattering experiment [90] (top right). The occupation density through a (001) plane at $k_z = 0.48\,(\pi / a)$, where brighter shades represent a higher occupation is shown (bottom) together with a contour of this occupation density at the level corresponding to the Fermi energy.

tively sharp. From an experiment which involved the measurement of 24 Compton profiles of a $Ni_{0.68}Al_{0.32}$ single crystal along directions which were specially chosen to be particularly efficient for the Jacobi-polynomial-based reconstruction method [15,91], Watts *et al.* were able to obtain the Fermi surface [90]. In Fig. 9, the Fermi surface predicted by KKR calculations is compared with the experimentally obtained one. The agreement is rather good, with the exception of a neck which appears to touch the Brillouin zone at the X point which is not present by the theory. Importantly for the nesting hypothesis, however, the nested region of the Fermi surface, which is most easily observed in a (100) plane at $k_z = 0.48\,(\pi / a)$ (also shown in Fig. 9), is very well predicted by the KKR–CPA theory. Given that the CPA is a mean-field theory, it is perhaps not too surprising that the agreement is not perfect, and non-local-CPA calculations might prove interesting [92].

9.2. $Ni_{1-x}Ti_x$

NiTi is unequivocally the most technologically exploited shape-memory alloy. Inelastic neutron scattering in the high-temperature phase found a temperature-dependent softening of the TA_2 [110] phonon branch near a q vector of 1/3 [110] $2\pi/a$ [93,94], this being a nesting vector in the Fermi surface calculated by Zhao and Harmon [95] (and which gives rise to an instability in their calculated phonon spectrum). By measuring Compton profiles along 28 different crystallographic directions in a single crystal of $Ni_{0.515}Ti_{0.485}$, and then reconstructing them using a direct Fourier method [96], Shiotani *et al.* were able to infer the Fermi surface [97]. In contrast to $Ni_{1-x}Al_x$, the nested regions of Fermi surface are harder to see directly, and while the overall Fermi surface topology is very close to that predicted by Zhao and Harmon, they do point out some discrepancies (which could be due to the treatment, or rather the lack of treatment of the substitutional disorder).

9.3. Ni_2MnGa

Heating and cooling through an martensitic transformation is often too slow for non-magnetic shape-memory materials to be used as actuators. This has led to an intense search for and development of materials, such as Ni_2MnGa, where structural changes can be induced by an external magnetic field [98]. Stoichiometric Ni_2MnGa is ferromagnetic below $T_C \sim 380$ K and undergoes a transition from the cubic $L2_1$ phase to a modulated tetragonal structure with $c/a = 0.97$ at $T_M \sim 220$ K [99,100].

There has been substantial theoretical work on the role of the Fermi surface in this material. Velikokhatnyi and Naumov [101] studied the Fermi surface of Ni_2MnGa for nesting instabilities and identified a number of possible nesting vectors which could play roles in the martensitic and premartensitic transitions. But, as pointed out by Lee *et al.*, within a simple Stoner picture of the magnetism, the exchange splitting, magnetic moment and Fermi surface is evolving with temperature, below the Curie temperature [102]. Using this simple picture, they were able to make calculations of the generalized susceptibility as a function of magnetization (and thus temperature) and show that at the temperature of the premartensitic transition, there was substantial Fermi surface nesting [102]. First principles calculations of the lattice instabilities were performed by Bungaro and Rabe [103], but some vectors identified in the Fermi surface topology do not appear to be proper nesting vectors.

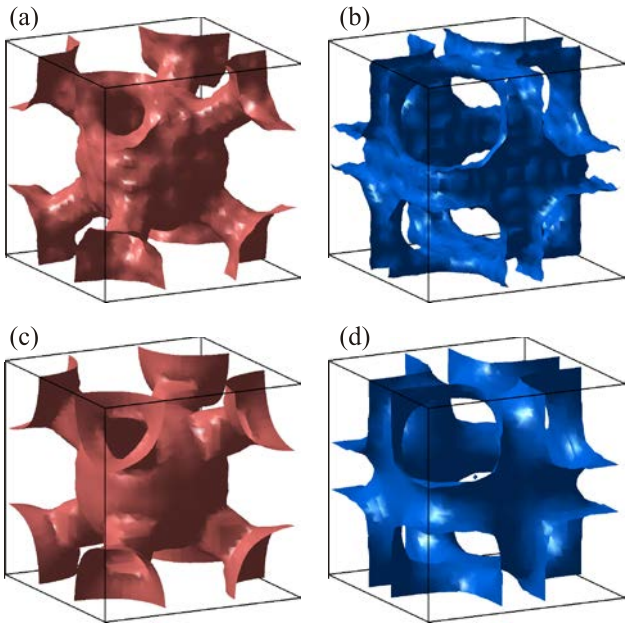

Fig. 10. (Color online) Experiment and theory for Ni_2MnGa. (a) and (b) show isosurfaces of the 3D tomographic reconstructions of 2D-ACAR data, determined from discontinuities in the 3D momentum density. (c) and (d) display the expected contours from the theory, which were extracted in the same way as the experimental contours and includes the expected Fermi broadening.

A positron annihilation study by Haynes *et al.* [104] has helped to clarify the Fermi surface topology. Haynes *et al.* were able to make a full three-dimensional reconstruction of the Fermi surface at 300 K from six measured projections. A visualization of the resulting Fermi surface is shown in Fig. 10, together with that from theoretical calculations. A careful analysis of the experimental densities, and comparison with the corresponding theoretical ones helped Haynes *et al.* identify the nested sheets of Fermi surface suggested by Entel *et al.* [105] and Lee *et al.* [102].

10. Organic conductors

Tetrathiafulvalere–tetracyan/quinodimethan (TTF–TCNQ) is an organic conductor [106]. Although the traditional LCW analysis could not resolve a Fermi surface due to the finite resolution, large unit cell (and therefore small Brillouin zone), or possible trapping due to defects created by the radiation, Ishibashi *et al.* used Compton scattering to study

the momentum density in [107] and demonstrated the sensitivity of the Compton technique to the differences in the descriptions of the electronic wavefunctions used in the molecular orbital calculations. Reasonable agreement was demonstrated between the measured anisotropy in the Compton profiles along different crystallographic directions and molecular orbital calculations in which TTF and TCNQ were treated as separate molecules and their results superposed, but the best agreement was with a band structure calculation.

In bis-tetramethyl-tetraselenofulvalene perchlorate ($(TMTSF)_2ClO_4$, where TMSF is $(CH_3)_4C_6Se_4$) Ishibashi *et al.* were able to resolve a step-like structure in their LCW-folded data [108], but they were not able to unambiguously determine whether this was a Fermi surface or not.

11. Superconductors

Both positron annihilation and Compton scattering have been able to make substantial contributions to our understanding of the electronic structure of superconductors.

11.1. High-temperature superconductors

Already with the A15 materials, (Nb_3Sn [109], V_3Si [110,111]) positron annihilation was beginning to emerge as an important tool for Fermi surface studies in superconductors. There was a tremendous surge of activity following the discovery of high-temperature superconductivity in the cuprates, as discussed in the comprehensive review by Peter *et al.* [112]. One of the significant challenges encountered in the experiments on $YBa_2Cu_3O_7$ was the unavoidable (Coulomb-driven) preference of the positron for the Cu–O chains over the Cu–O_2 planes. Sampling all electrons equally, Compton scattering does not suffer from this drawback, and has recently been used to probe the orbital character of holes doped into $La_{2x}Sr_xCuO_4$ [113]. In a combined experimental and theoretical *tour de force*, Sakurai *et al.* were able to show that on the underdoped side of the phase diagram, the holes were primarily in the O $2p_x/p_y$ orbitals, but on the overdoped side they mostly dope into the Cu d orbitals. Robust from surface effects, defects or impurities, Compton scattering was shown to be a powerful probe of the orbital character of dopants in electronically complex materials.

11.2. Hydrated Na *cobaltates*

The discovery [114] of superconductivity at 5 K in hydrated Na_xCoO_2 was quickly followed by theoretical speculation about the role of Fermi surface nesting [115], and a series of attempts to measure the Fermi surface (see, for example, [116–118]). A controversy quickly emerged regarding the possible existence of e'_g pockets (which were not observed in the ARPES experiments) but which were predicted by LDA calculations [119,120]. A bulk measurement was therefore highly desirable and Laverock *et al.* made a series of Compton scattering measurements in samples with different hole concentrations, including a sample which had been hydrated and was of a composition which exhibited superconductivity [121].

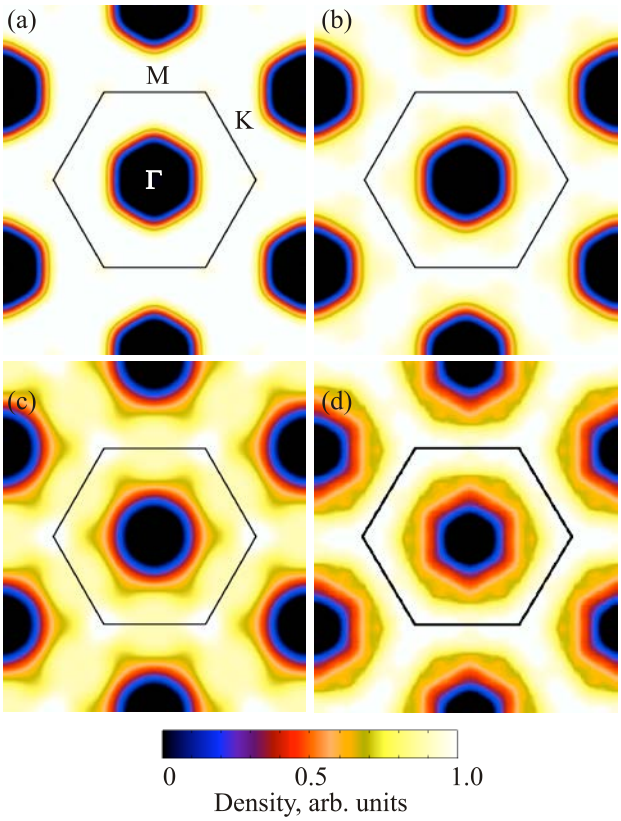

Fig. 11. (Color online) The experimental Fermi surface of Na_xCoO_2 for (a) x = 0.74, (b) 0.51, (c) 0.38, and (d) for $Na_{0.35}CoO_2{\cdot}1.3D_2O$ obtained from the reconstruction of five Compton profiles for each composition. The boundary of the first Brillouin zone is indicated.

They were able to show (Fig. 11) that at lower Na concentrations (lower x) in a bulk Fermi surface measurement, that the small e'_g pockets did indeed exist, raising the strong possibility that the surfaces of these materials are not representative of the bulk.

Concluding remarks

When looking for a bulk Fermi surface spectroscopy for materials where the electronic mean-free-paths are too short for the observation of quantum oscillations (due to substitutional disorder, high temperature phases etc.) positron annihilation and Compton scattering are viable techniques. Accessing the Fermi surface through the underlying electron momentum distribution, these techniques have revealed electronic structure of a diverse range of materials and provided unique insight into a variety of phenomena ranging from aspects of superconductivity through density-waves to heavy fermions.

1. D.G. Lock, V.H.C. Crisp, and R.N. West, *J. Phys. F* **3**, 561 (1973).
2. T. Jarlborg and A.K. Singh, *Phys. Rev. B* **36**, 4660 (1987).
3. N.D. Drummond, P. Lopez Rios, R.J. Needs, and C.J. Pickard, *Phys. Rev. Lett.* **107**, 207402 (2011).
4. J. Laverock, T.D. Haynes, M.A. Alam, and S.B. Dugdale, *Phys. Rev. B* **82**, 125127 (2010).
5. B. Barbiellini, M.J. Puska, T. Korhonen, A. Harju, T. Torsti, and R.M. Nieminen, *Phys. Rev. B* **53**, 16201 (1996).
6. J. Mitroy and B. Barbiellini, *Phys. Rev. B* **65**, 235103 (2002).
7. N. Hiraoka, M. Itou, T. Ohata, M. Mizumaki, Y. Sakurai, and N. Sakai, *J. Synch. Radiat.* **8**, 26 (2001).
8. Y. Sakurai and M. Itou, *J. Phys. Chem. Solids* **65**, 2061 (2004).
9. S.B. Dugdale, J. Laverock, C. Utfeld, M.A. Alam, T.D. Haynes, D. Billington, and D. Ernsting, *J. Phys.: Conf. Ser.* **443**, 012083 (2013).
10. R.N. West, J. Mayers, and P.A. Walters, *J. Phys. E* **14**, 478 (1981).
11. M. Leitner, H. Ceeh, and J.-A. Weber, *New J. Phys.* **14**, 123014 (2012).
12. A.M. Cormack, *J. Appl. Phys.* **35**, 2908 (1964).
13. A.M. Cormack, *J. Appl. Phys.* **34**, 2722 (1963).
14. G. Kontrym-Sznajd, *Phys. Status Solidi A* **117**, 227 (1990).
15. G. Kontrym-Sznajd, A. Jura, and M. Samsel-Czekala, *Appl. Phys. A* **74**, 605 (2002).
16. W.E. Evenson and S.H. Liu, *Phys. Rev.* **178**, 783 (1969).
17. I.D. Hughes, M. Daene, A. Ernst, W. Hergert, M. Lueders, J. Poulter, J.B. Staunton, A. Svane, Z. Szotek, and W.M. Temmerman, *Nature* **446**, 650 (2007).
18. T.L. Loucks, *Phys. Rev.* **144**, 504 (1966).
19. S.B. Dugdale, H.M. Fretwell, M.A. Alam, G. Kontrym-Sznajd, R.N. West, and S. Badrzadeh, *Phys. Rev. Lett.* **79**, 941 (1997).
20. H.M. Fretwell, S.B. Dugdale, M.A. Alam, D.C.R. Hedley, A. Rodriguez-Gonzalez, and S.B. Palmer, *Phys. Rev. Lett.* **82**, 3867 (1999).
21. S.J. Crowe, S.B. Dugdale, Z. Major, M.A. Alam, J.A. Duffy, and S.B. Palmer, *Europhys. Lett.* **65**, 235 (2004).
22. W.C. Koehler, *J. Appl. Phys.* **36**, 1078 (1965).
23. G. Kontrym-Sznajd, M. Samsel-Czekala, A. Pietraszko, H. Sormann, S. Manninen, S. Huo-tari, K. Hämäläinen, J. Laukkanen, R.N. West, and W. Schülke, *Phys. Rev. B* **66**, 155110 (2002).
24. Z. Major, S.B. Dugdale, R.J. Watts, G. Santi, M.A. Alam, S.M. Hayden, J.A. Duffy, J.W. Taylor, T. Jarlborg, E. Bruno, D. Benea, and H. Ebert, *Phys. Rev. Lett.* **92**, 107003 (2004).
25. C. Pfleiderer, M. Uhlarz, S. Hayden, R. Vollmer, H. von Lohneysen, N. Bernhoeft, and G. Lonzarich, *Nature* **412**, 58 (2001).
26. S. Saxena, P. Agarwal, K. Ahilan, F. Grosche, R. Haselwimmer, M. Steiner, E. Pugh, I. Walker, S. Julian, P. Monthoux, G. Lonzarich, A. Huxley, I. Sheikin, D. Braithwaite, and J. Flouquet, *Nature* **406**, 587 (2000).
27. D. Fay and J. Appel, *Phys. Rev. B* **22**, 3173 (1980).
28. G. Santi, S.B. Dugdale, and T. Jarlborg, *Phys. Rev. Lett.* **87**, 247004 (2001).
29. S.J.C. Yates, G. Santi, S.M. Hayden, P.J. Meeson, and S.B. Dugdale, *Phys. Rev. Lett.* **90**, 057003 (2003).
30. E.A. Yelland, S.M. Hayden, S.J.C. Yates, C. Pfleiderer, M. Uhlarz, R. Vollmer, H. v. Löhneysen, N.R. Bernhoeft, R.P. Smith, S.S. Saxena, and N. Kimura, *Phys. Rev. B* **72**, 214523 (2005).
31. S.C. Moss, *Phys. Rev. Lett.* **22**, 1108 (1969).
32. M. Rodewald, K. Rodewald, P. De Meulenaere, and G. Van Tendeloo, *Phys. Rev. B* **55**, 14173 (1997).
33. B.L. Gyorffy and G.M. Stocks, *Phys. Rev. Lett.* **50**, 374 (1983).
34. I. Wilkinson, R.J. Hughes, Z. Major, S.B. Dugdale, M.A. Alam, E. Bruno, B. Ginatempo, and E.S. Giuliano, *Phys. Rev. Lett.* **87**, 216401 (2001).
35. P. Soven, *Phys. Rev.* **156**, 809 (1967).
36. I. Matsumoto, H. Kawata, and N. Shiotani, *Phys. Rev. B* **64**, 195132 (2001).
37. J. Friedel and M. Peter, *Europhys. Lett.* **8**, 79 (1989).
38. R.E. Peierls, *Quantum Theory of Solids*, Oxford University, New York/London (1955).
39. J.A. Wilson, F.J. Di Salvo, and S. Mahajan, *Adv. Phys.* **50**, 1171 (2001).
40. B. Mansart, M.J.G. Cottet, T.J. Penfold, S.B. Dugdale, R. Tediosi, M. Chergui, and F. Carbone, *Proc. Natl. Acad. Sci.* **109**, 5603 (2012).
41. J. Laverock, T.D. Haynes, C. Utfeld, and S.B. Dugdale, *Phys. Rev. B* **80**, 125111 (2009).
42. M.D. Johannes and I.I. Mazin, *Phys. Rev. B* **77**, 165135 (2008).
43. J. Laverock, D. Newby, E. Abreu, R. Averitt, K.E. Smith, R.P. Singh, G. Balakrishnan, J. Adell, and T. Balasubramanian, *Phys. Rev. B* **88**, 035108 (2013).
44. N. Ru, C.L. Condron, G.Y. Margulis, K.Y. Shin, J. Laverock, S.B. Dugdale, M.F. Toney, and I.R. Fisher, *Phys. Rev. B* **77**, 035114 (2008).
45. V. Brouet, W.L. Yang, X.J. Zhou, Z. Hussain, N. Ru, K.Y. Shin, I.R. Fisher, and Z.X. Shen, *Phys. Rev. Lett.* **93**, 126405 (2004).
46. V. Brouet, W.L. Yang, X.J. Zhou, Z. Hussain, R.G. Moore, R. He, D.H. Lu, Z.X. Shen, J. Laverock, S.B. Dugdale, N. Ru, and I.R. Fisher, *Phys. Rev. B* **77**, 235104 (2008).
47. E. DiMasi, M.C. Aronson, J.F. Mansfield, B. Foran, and S. Lee, *Phys. Rev. B* **52**, 14516 (1995).
48. J. Laverock, S.B. Dugdale, Z. Major, M.A. Alam, N. Ru, I.R. Fisher, G. Santi, and E. Bruno, *Phys. Rev. B* **71**, 085114 (2005).
49. E. Fawcett, *Rev. Mod. Phys.* **60**, 209 (1988).
50. A.W. Overhauser, *Phys. Rev. Lett.* **4**, 462 (1960).
51. A.W. Overhauser, *Phys. Rev.* **128**, 1437 (1962).
52. W.M. Lomer, *Proc. Phys. Soc.* **80**, 489 (1962).
53. N. Shiotani, T. Okada, H. Sekizawa, S. Wakoh, and Y. Kubo, *J. Phys. Soc. Jpn.* **43**, 1229 (1977).
54. A.K. Singh, A.A. Manuel, and E. Walker, *Europhys. Lett.* **6**, 67 (1988).
55. T. Kubota, H. Kondo, H. Nakashima, Y. Murakami, and S. Tanigawa, *Phys. Status Solidi B* **168**, 179 (1991).
56. S.B. Dugdale, M.A. Alam, H.M. Fretwell, M. Biasini, and D. Wilson, *J. Phys.: Condens. Matter* **6**, L435 (1994).

57. H.M. Fretwell, S.B. Dugdale, M.A. Alam, M. Biasini, L. Hoffmann, and A.A. Manuel, *Europhys. Lett.* **32**, 771 (1995).
58. S.B. Dugdale, H.M. Fretwell, D.C.R. Hedley, M.A. Alam, T. Jarlborg, G. Santi, R.M. Singru, V. Sundararajan, and M.J. Cooper, *J. Phys.: Condens. Matter* **10**, 10367 (1998).
59. S.B. Dugdale, H.M. Fretwell, K.J. Chen, Y. Tanaka, A. Shukla, T. Buslaps, C. Bellin, G. Loupias, M.A. Alam, A.A. Manuel, P. Suortti, and N. Shiotani, *J. Phys. Chem. Solids* **61**, 361 (2000).
60. Y. Tanaka, K.J. Chen, C. Bellin, G. Loupias, H.M. Fretwell, A. Rodrigues-Gonzalez, M.A. Alam, S.B. Dugdale, A.A. Manuel, A. Shukla, T. Buslaps, P. Suortti, and N. Shiotani, *J. Phys. Chem. Solids* **61**, 365 (2000).
61. R.J. Hughes, S.B. Dugdale, Z. Major, M.A. Alam, T. Jarlborg, E. Bruno, and B. Ginatempo, *Phys. Rev. B* **69**, 174406 (2004).
62. P. Grünberg, R. Schreiber, Y. Pang, M.B. Brodsky, and H. Sowers, *Phys. Rev. Lett.* **57**, 2442 (1986).
63. S.S.P. Parkin, N. More, and K.P. Roche, *Phys. Rev. Lett.* **64**, 2304 (1990).
64. M. Biasini, G. Ferro, and A. Czopnik, *Phys. Rev. B* **68**, 094513 (2003).
65. T. Ebihara, I. Umehara, A. Albessard, K. Satoh, and Y. Onuki, *Physica B* **186–188**, 123 (1993).
66. O. Sakai and H. Harima, *J. Phys. Soc. Jpn.* **81**, 024717 (2012).
67. M.J. Besnus, J.P. Kappler, P. Lehmann, and A. Meyer, *Solid State Commun.* **55**, 779 (1985).
68. M.A. Monge, M. Biasini, G. Ferro, M. Gemmi, G. Satta, S. Massidda, P. Lejay, and A. Continenza, *Phys. Rev. B* **65**, 035114 (2002).
69. Y. Onuki, I. Umehara, A.K. Albessard, T. Ebihara, and K. Satoh, *J. Phys. Soc. Jpn*. **61**, 960 (1992).
70. A.I. Coldea, J.D. Fletcher, A. Carrington, J.G. Analytis, A.F. Bangura, J.-H. Chu, A.S. Erickson, I.R. Fisher, N.E. Hussey, and R.D. McDonald, *Phys. Rev. Lett.* **101**, 216402 (2008).
71. C. Utfeld, J. Laverock, T.D. Haynes, S.B. Dugdale, J.A. Duffy, M.W. Butchers, J.W. Taylor, S.R. Giblin, J.G. Analytis, J.-H. Chu, I.R. Fisher, M. Itou, and Y. Sakurai, *Phys. Rev. B* **81**, 064509 (2010).
72. Z. Major, S.B. Dugdale, R.J. Watts, J. Laverock, J.J. Kelly, D.C.R. Hedley, and M.A. Alam, *J. Phys. Chem. Solids* **65**, 2011 (2004).
73. C. Utfeld, S.R. Giblin, J.W. Taylor, J.A. Duffy, C. Shenton-Taylor, J. Laverock, S.B. Dugdale, M. Manno, C. Leighton, M. Itou, and Y. Sakurai, *Phys. Rev. Lett.* **103**, 226403 (2009).
74. F.S. Tautz, S.R. Julian, G.J. McMullan, and G.G. Lonzarich, *Physica B* **206**–**207**, 29 (1995).
75. D. Vasumathi, B. Barbiellini, A.A. Manuel, L. Hoffmann, T. Jarlborg, R. Modler, C. Geibel, F. Steglich, and M. Peter, *Phys. Rev. B* **55**, 11714 (1997).
76. M.J. Puska, P. Lanki, and R.M. Nieminen, *J. Phys.: Condens. Matter* **1**, 6081 (1989).
77. Y. Nagai, T. Chiba, Z. Tang, T. Akahane, T. Kanai, M. Hasegawa, M. Takenaka, and E. Kuramoto, *Phys. Rev. Lett.* **87**, 176402 (2001).
78. Y. Nagai, M. Hasegawa, Z. Tang, A. Hempel, K. Yubuta, T. Shimamura, Y. Kawazoe, A. Kawai, and F. Kano, *Phys. Rev. B* **61**, 6574 (2000).
79. Y. Nagai, T. Toyama, Z. Tang, K. Inoue, T. Chiba, M. Hasegawa, S. Hirosawa, and T. Sato, *Phys. Rev. B* **79**, 201405 (2009).
80. T. Toyama, Z. Tang, K. Inoue, T. Chiba, T. Ohkubo, K. Hono, Y. Nagai, and M. Hasegawa, *Phys. Rev. B* **86**, 104106 (2012).
81. M. Sluiter, D. de Fontaine, X.Q. Guo, R. Podloucky, and A.J. Freeman, *Phys. Rev. B* **42**, 10460 (1990).
82. K. Mahalingam, B.P. Gu, G.L. Liedl, and T.H. Sanders Jr, *Acta Metallurg.* **35**, 483 (1987).
83. J. Laverock, S.B. Dugdale, M.A. Alam, M.V. Roussenova, J.R. Wensley, J. Kwiatkowska, and N. Shiotani, *Phys. Rev. Lett.* **105**, 236401 (2010).
84. X.-Q. Guo, R. Podloucky, J.-h. Xu, and A.J. Freeman, *Phys. Rev. B* **41**, 12432 (1990).
85. P.A. Goddard, J. Singleton, R.D. McDonald, N. Harrison, J.C. Lashley, H. Harima, and M.-T. Suzuki, *Phys. Rev. Lett.* **94**, 116401 (2005).
86. R.D. McDonald, P.A. Goddard, J. Lashley, N. Harrison, C.H. Mielke, J. Singleton, H. Harima, and M.-T. Suzuki, *J. Phys. Chem. Solids* **67**, 2100 (2006).
87. W. Kohn, *Phys. Rev. Lett.* **2**, 393 (1959).
88. S.M. Shapiro, B.X. Yang, Y. Noda, L.E. Tanner, and D. Schryvers, *Phys. Rev. B* **44**, 9301 (1991).
89. G.L. Zhao and B.N. Harmon, *Phys. Rev. B* **45**, 2818 (1992).
90. S.B. Dugdale, R.J. Watts, J. Laverock, Z. Major, M.A. Alam, M. Samsel-Czekala, G. Kontrym-Sznajd, Y. Sakurai, M. Itou, and D. Fort, *Phys. Rev. Lett.* **96**, 046406 (2006).
91. G. Kontrym-Sznajd and M. Samsel-Czekala, *Appl. Phys. A* **70**, 89 (2000).
92. A. Marmodoro and J.B. Staunton, *J. Phys.: Conf. Ser.* **286**, 012033 (2011).
93. H. Tietze, M. Müllner, and B. Renker, *J. Phys. C* **17**, L529 (1984).
94. P. Moine, J. Allain, and B. Renker, *J. Phys. F* **14**, 2517 (1984).
95. G.L. Zhao and B.N. Harmon, *Phys. Rev. B* **48**, 2031 (1993).
96. R. Suzuki, M. Osawa, S. Tanigawa, M. Matsumoto, and N. Shiotani, *J. Phys. Soc. Jpn.* **58**, 3251 (1989).
97. N. Shiotani, I. Matsumoto, H. Kawata, J. Katsuyama, M. Mizuno, H. Araki, and Y. Shirai, *J. Phys. Soc. Jpn.* **73**, 1627 (2004).
98. K. Ullakko, J.K. Huang, C. Kantner, R.C. OHandley, and V.V. Kokorin, *Appl. Phys. Lett.* **69**, 1966 (1996).
99. P.J. Webster, K.R.A. Ziebeck, S.L. Town, and M.S. Peak, *Philos. Mag. B* **49**, 295 (1984).
100. A. Zheludev, S.M. Shapiro, P. Wochner, and L.E. Tanner, *Phys. Rev. B* **54**, 15045 (1996).
101. O. Velikokhatnyi and I. Naumov, *Phys. Solid State* **41**, 617 (1999).
102. Y. Lee, J.Y. Rhee, and B.N. Harmon, *Phys. Rev. B* **66**, 054424 (2002).
103. C. Bungaro, K.M. Rabe, and A.D. Corso, *Phys. Rev. B* **68**, 134104 (2003).

104. T.D. Haynes, R.J. Watts, J. Laverock, Z. Major, M.A. Alam, J.W. Taylor, J.A. Duffy, and S.B. Dugdale, *New J. Phys.* **14**, 035020 (2012).
105. P. Entel, A. Dannenberg, M. Siewert, H. Herper, M. Gruner, D. Comtesse, H.-J. Elmers, and M. Kallmayer, *Metallurg. Mater. Transact. A* **43**, 2891 (2012).
106. S. Ishibashi, A.A. Manuel, L. Hoffmann, and K. Bechgaard, *Phys. Rev. B* **55**, 2048 (1997).
107. S. Ishibashi, A.A. Manuel, D. Vasumathi, A. Shukla, P. Suortti, M. Kohyama, and K. Bechgaard, *J. Phys.: Condens. Matter* **11**, 9025 (1999).
108. S. Ishibashi, A.A. Manuel, M. Kohyama, M. Tokumoto, and H. Anzai, *Phys. Rev. B* **60**, R 3747 (1999).
109. L. Hoffmann, A.K. Singh, H. Takei, and N. Toyota, *J. Phys. F* **18**, 2605 (1988).
110. A.A. Manuel, *Phys. Rev. Lett.* **49**, 1525 (1982).
111. T. Jarlborg, A.A. Manuel, and M. Peter, *Phys. Rev. B* **27**, 4210 (1983).
112. M. Peter, A.A. Manuel, and A. Erb, *Intern. J. Modern Phys. B* **12**, 3187 (1998).
113. Y. Sakurai, M. Itou, B. Barbiellini, P.E. Mijnarends, R.S. Markiewicz, S. Kaprzyk, J.-M. Gillet, S. Wakimoto, M. Fujita, S. Basak, Y.J. Wang, W. Al-Sawai, H. Lin, A. Bansil, and K. Yamada, *Science* **332**, 698 (2011).
114. K. Takada, H. Sakurai, E. Takayama-Muromachi, F. Izumi, R. Dilanian, and T. Sasaki, *Nature* **422**, 53 (2003).
115. I. Mazin and M. Johannes, *Nature Phys.* **1**, 91 (2005).
116. M.Z. Hasan, Y.-D. Chuang, D. Qian, Y.W. Li, Y. Kong, A. Kuprin, A.V. Fedorov, R. Kimmerling, E. Rotenberg, K. Rossnagel, Z. Hussain, H. Koh, N.S. Rogado, M.L. Foo, and R.J. Cava, *Phys. Rev. Lett.* **92**, 246402 (2004).
117. H.-B. Yang, S.-C. Wang, A.K.P. Sekharan, H. Matsui, S. Souma, T. Sato, T. Takahashi, T. Takeuchi, J.C. Campuzano, R. Jin, B.C. Sales, D. Mandrus, Z. Wang, and H. Ding, *Phys. Rev. Lett.* **92**, 246403 (2004).
118. H.-B. Yang, Z.-H. Pan, A.K.P. Sekharan, T. Sato, S. Souma, T. Takahashi, R. Jin, B.C. Sales, D. Mandrus, A.V. Fedorov, Z. Wang, and H. Ding, *Phys. Rev. Lett.* **95**, 146401 (2005).
119. D.J. Singh, *Phys. Rev. B* **61**, 13397 (2000).
120. K.-W. Lee, J. Kuneš, and W.E. Pickett, *Phys. Rev. B* **70**, 045104 (2004).
121. J. Laverock, S.B. Dugdale, J.A. Duffy, J. Wooldridge, G. Balakrishnan, M.R. Lees, G.-q. Zheng, D. Chen, C.T. Lin, A. Andrejczuk, M. Itou, and Y. Sakurai, *Phys. Rev. B* **76**, 052509 (2007).